Rock and Soil Mechanics

Volume 41 | Issue 3 Article 5

9-27-2020

Study on the influence of bedding plane on the fracturing behavior of sandstone

Bin LI
State Key Laboratory for Coal Mine Disaster Dynamics and Control, Chongqing University, Chongqing 400044, China

Da HUANG
School of Civil Engineering and Transportation, Hebei University of Technology, Tianjin 300401, China

Wen-zhu MA
School of Civil Engineering and Transportation, Hebei University of Technology, Tianjin 300401, China

Custom Citation

LI Bin, HUANG Da, MA Wen-zhu, . Study on the influence of bedding plane on the fracturing behavior of sandstone[J]. Rock and Soil Mechanics, 2020, 41(3): 858-868.

Rock and Soil Mechanics 2020 41(3): 858−868 ISSN 1000−7598
https: //doi.org/10.16285/j.rsm.2019.5643 rocksoilmech.researchcommons.org/journal

Study on the influence of bedding plane on the fracturing behavior of sandstone

LI Bin[1], HUANG Da[1, 2], MA Wen-zhu[2]
1. State Key Laboratory for Coal Mine Disaster Dynamics and Control, Chongqing University, Chongqing 400044, China
2. School of Civil Engineering and Transportation, Hebei University of Technology, Tianjin 300401, China

Abstract: The mechanical behavior of layered stone is much influenced by the weak bedding planes. To further explore how the layered structure influences the fracture characteristic of layered sandstone, a series of three-point-bending tests on sandstone specimens with different inclination angles was conducted and the anisotropy of fracture toughness and fracture pattern were discussed. Then a numerical model based on cohesive elements was proposed to simulate the fracture of semi-circular sandstone specimens under three-point-bending test and the effects of bedding strength on the fracturing behavior of semi-circular bending(SCB) specimens with different inclination angles were discussed by simulation with the proposed model. The results show that fracture toughness and fracture pattern are anisotropic under the influence of the inclination angle of the bedding, and fracture toughness increases with the increase of bedding strength for a fixed inclination angle. In addition, the influence of joint strength on the fracture toughness is greater for lower inclination angles and the fracture patterns are not only influenced by joint strength, but also related to the inclination angle. Fracture patterns of $\theta = 0^{\circ}$ specimens are almost not influenced by the joint strength, and the specimens all split along the bedding plane with tensile failure; tensile or shearing failure along the bedding plane occurs on $\theta = 30^{\circ}$ specimens and the crack length along the bedding plane increases with the decrease of joint strength; when the joint strength is higher, tensile failure along the bedding plane occurs on $\theta = 45^{\circ}$ specimens and tensile failure crossing the bedding plane occurs on $\theta = 60^{\circ}$−90° specimens, while shearing failure along the bedding plane occurs on $\theta = 45^{\circ}$−90° specimens when the joint strength becomes lower. Furthermore, the maximum shearing length occurs on $\theta = 45^{\circ}$ specimens. In addition, the impacts on the crack initiation angle and crack propagation path caused by both bedding strength and inclination angle are discussed based on the numerical results. The findings in this paper may enrich the theory of fracture mechanics on layered rock.

Keywords: semi-circular sandstone specimen; three-point-bending test; cohesive element; bedding orientation; bedding strength; fracturing behaviour

1 Introduction

Massive weak bedding planes, which are strongly affected by sedimentation, stress and hydrogeology conditions during the diagenetic process, are often found in sedimentary rocks such as sandstone. Experiments[1−7] demonstrated a large difference in mechanical properties and failure patterns of rocks with different bedding planes. The brittle failure of rocks in various engineering (e.g., energy exploitation, slope and underground engineering) always involves fracture behaviour of layered rocks which are widely distributed. Therefore, it is of significant importance to understand the effect of bedding planes on fracture behaviors of rocks.

The fracture toughness, which is a crucial strength index of rock fracture mechanical behavior, is used to describe the resistance to initiation and propagation of fractures in the rock. The three-point-bending tests on notched specimens are always applied to measure the fracture toughness. The semi-circular bending (SCB) test suggested by the ISRM, which owns the advantages of easy sample preparation, simple testing apparatus and procedure, is widely used by researchers[8−12]. The fracture toughness of anisotropic or layered rocks can also be measured by SCB tests[13−16]. In addition, many theoretical and experimental studies about specific parameters (e.g., dimensions, crack-to-radius ratio, loading rate, mineral composition and temperature) on fracture toughness have been conducted[17−19]. However, the effects of bedding characteristics on the fracture behavior of layered rocks are still not clear. As a beneficial supplement to experiments, numerical simulations based on rock mechanics test is not only helpful for further understanding the experimental results, but also revealing the mechanism and rules of rock failure. The discrete element codes such as PFC and UDEC were adopted to simulate the fracture and crack propagation[20−22]. However, the discrete element method (DEM) often uses rigid discs or spheres to approximately represent the micro-structure of rocks, which may lead to inaccurate results. The finite element method (FEM) uses the failure and disappearance of cohesive elements to simulate the fracture and failure of rock materials. It avoids the weakness of DEM and has been applied in the simulation of rock fracture[23−27].

In this study, three-point-bending tests on semi-circular sandstone specimens with different layer orientations were conducted to obtain the fracture toughness and failure pattern.

Received: 8 April 2019 Revised: 22 August 2019
This work was supported by the National Natural Science Foundation of China(41672300).
First author: LI Bin, male, born in 1988, PhD candidate, focusing on rock mechanics and rock slope engineering. E-mail: 15683086591@163.com

Furthermore, based on the cohesive element method (CEM) of finite element code, 3D numerical models of the semi-circular specimens were set up to investigate the fracture behavior of layered sandstone. The numerical results were then verified by experimental results and the effects of bedding strength on fracture behaviors were numerically investigated. The research results in this paper can provide theoretical basis and technical support for fracture initiation and propagation in layered rocks.

2 Three-point-bending tests on sandstone with bedding planes

2.1 Test material and procedure

The sandstone specimens were manufactured from an intact rock block obtained from a construction engineering of Chongqing, China. The sandstone has a mean density of about 2.5 g/cm^3. It has massive bedding planes with a bedding spacing of about 1–2 mm. The uniaxial compression tests show that the uniaxial compression strength P is 38 MPa, Young's modulus is 15 GPa and the Poisson's ratio is 0.12 when the loading direction is perpendicular to the bedding planes. When the loading direction is parallel to the bedding planes, the uniaxial compression strength is 30 MPa, Young's modulus is 30 GPa and the Poisson's ratio is 0.2, respectively. In total, 20 semi-circular specimens with a diameter of 100 mm and a thickness of 20 mm are divided into five groups with different bedding planes. Each group has 4 specimens with different angle between the bedding planes and loading direction (0°, 30°, 45°, 60°, 90°). A vertical notch (i.e., parallel to the loading direction) with a width of 1.5 mm and a length of 10 mm was cut in the SCB specimens using a thin diamond circular saw with a thickness of 1 mm. The geometry of specimens and loading directions are shown in Fig.1(a). θ is the angle between the bedding plane and loading direction. The loading span is 2S=80 mm. Some prepared specimens are shown in Fig.1(b). The three-point-bending tests were conducted on the MTS815 test system at the institute of geotechnical engineering of Chongqing University (Fig.1(c)). All specimens were loaded at a rate of 0.02 mm/min under the displacement control mode.

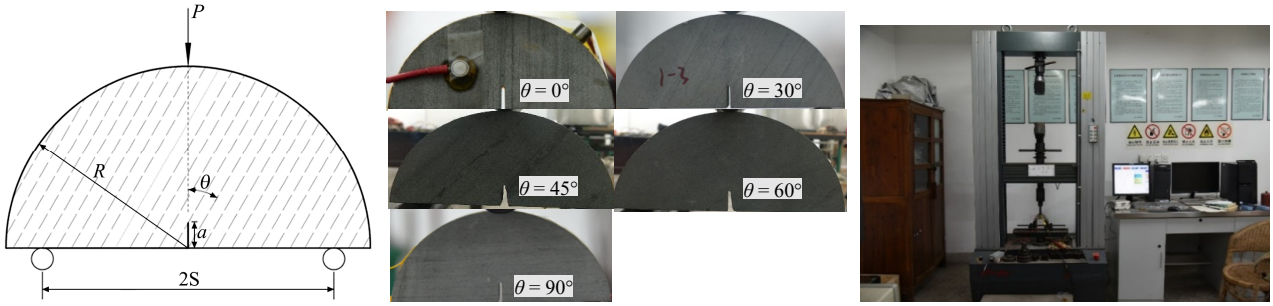

a-crack length; *R*-specimen radius; 2*S*-loading span; θ-the angle between bedding plane and loading direction

(a) Geometric parameters and loading direction (b) Specimens with different inclination angles (c) Test apparatus

Fig.1 SCB specimens and test machine

2.2 Experimental results

2.2.1 Anisotropy of fracture toughness

Based on the fracture load $P_{\max}$ tested by the SCB tests, the fracture toughness of specimens can be determined according to Eq.(1)[11]:

$$\left.\begin{aligned} K_{\mathrm{IC}} &= \frac{P_{\max}\sqrt{\pi a}}{2Rt}Y_{\mathrm{I}} \\ Y_{\mathrm{I}} &= -1.297+9.516\frac{S}{R}-\left(0.47+16.457\frac{S}{R}\right)\frac{a}{R}+ \\ &\quad \left(1.071+34.401\frac{S}{R}\right)\left(\frac{a}{R}\right)^2 \end{aligned}\right\} \tag{1}$$

where K_{IC} is the mode-I fracture toughness of specimen; Y_{I} is the dimensionless stress intensity factor; and t is specimen thickness.

The tested fracture toughness of specimens with different bedding inclination angles is shown in Fig.2. It can be seen that fracture toughness shows an obvious anisotropy with the variation of bedding inclination angles. The maximum fracture roughness occurs at θ=90° and the minimum fracture roughness occurs at θ=0° and it meets $K_{\max}/K_{\min}\approx 2.16$. $K_{\max}$ and $K_{\min}$ are the maximum and minimum values of fracture toughness, respectively. The fracture toughness increases with the increase of bedding inclination angles.

2.2.2 Anisotropy of fracture patterns

The fracture patterns of specimens with different inclination angles are shown in Fig.3. It can be seen that tensile failure occurs along the bedding planes of the specimens with θ=0° and θ=30°. The failure of specimens with θ=45° is dominated by fracture along the bedding planes. The fracture diverts towards the loading point after propagating along the bedding plane near the crack tip. The failure of specimens with θ=60° and θ=90° is dominated by tensile failure across the bedding planes. Fig.3(b) shows that the crack length along the bedding planes of specimens decreases with the increase of bedding inclination angles.

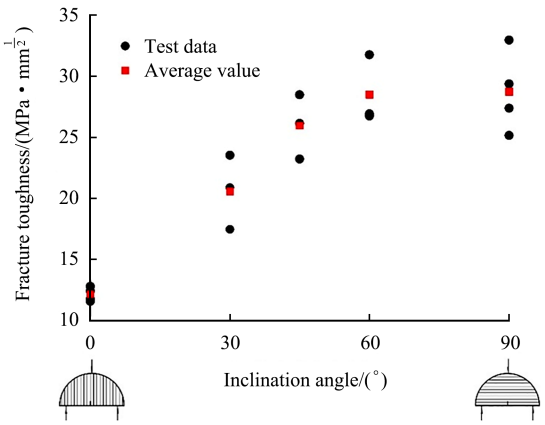

Fig.2 Test results of fracture toughness with different inclination angles

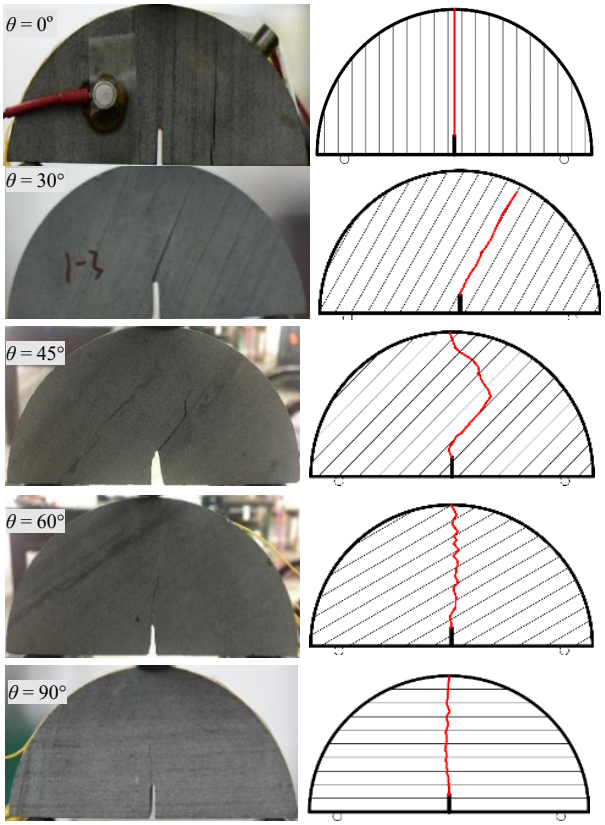

(a) Photos and sketch of fractured specimens

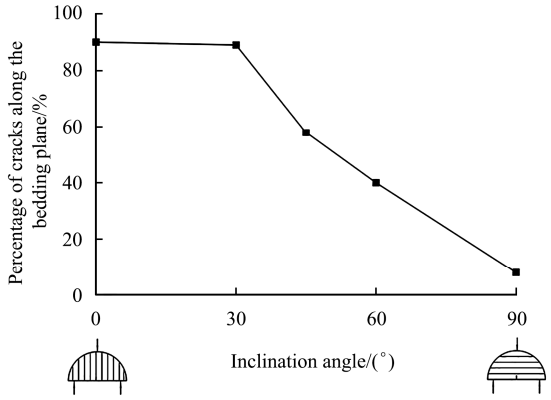

(b) Length percentage of cracks along the bedding planes

Fig.3 Fracture patterns of specimens with different inclination angles

3 Finite element numerical simulation based on cohesive elements

3.1 Cohesive elements with damage

Based on the bonding and aggregate interlocking between rock, concrete and asphalt, the cohesive element model assumes that there are a normal traction σ_n, and two tangential tractions σ_s and σ_t. These tractions decrease monotonically with the corresponding displacements of crack surfaces. Considering the anisotropy of fracture behavior caused by bedding orientation, the stress state on bedding planes is complicated. Therefore, a bilinear mixed-mode cohesive traction-separation constitutive is used to represent the cohesive elements of sandstone sample shown in Fig.4. σ_n^0, σ_s^0, σ_t^0 and σ_m^0 are the normal, longitudinal shear, transverse shear

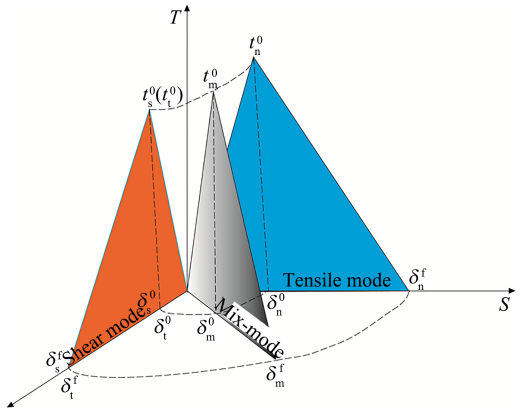

Fig.4 Mix-mode cohesive traction response

and effective tractions, respectively at the initiation of cracks. δ_n^0, δ_s^0, δ_t^0 and δ_m^0 are the normal, longitudinal shear, transverse shear and effective displacements of cohesive elements, respectively when the damage initiates. δ_n^f, δ_s^f, δ_t^f and δ_m^f are the normal, longitudinal shear, transverse shear and effective displacements of cohesive elements when tractions diminish and the cohesive elements fail. A damage variable D, which is related to the relative displacement of cohesive element, is introduced to represent the overall damage and it changes between 0 to 1 with load after the damage occurs. The stress damage functions of normal and shear tractions are as follows:

$$\left.\begin{aligned} t_n &= (1-D)t_n^0, t_n^0 \geqslant 0 \\ t_n &= t_n^0, t_n^0 < 0 \\ t_s &= (1-D)t_s^0 \\ t_t &= (1-D)t_t^0 \end{aligned}\right\} \tag{2}$$

where t_n^0, t_s^0 and t_t^0 are the initial normal, longitudinal shear and transverse shear tractions of cohesive elements, respectively. The normal, longitudinal shear and transverse shear stiffness k_n, k_s and k_t of the cohesive elements during the fracture propagation process can be expressed as

$$\left.\begin{aligned} k_{\mathrm{n}} &= (1-D)k_{\mathrm{n}}^{0} \\ k_{\mathrm{s}} &= (1-D)k_{\mathrm{s}}^{0} \\ k_{\mathrm{t}} &= (1-D)k_{\mathrm{t}}^{0} \end{aligned}\right\} \tag{3}$$

where k_{n}^{0}, k_{s}^{0} and k_{t}^{0} are the initial normal, longitudinal shear and transverse shear stiffness of cohesive elements, respectively.

To describe the damage evolution of cracks under a combination of normal and shear deformation, the effective displacement is written as follows:

$$\delta_{\mathrm{m}} = \sqrt{\langle \delta_{\mathrm{n}} \rangle^{2} + \delta_{\mathrm{s}}^{2} + \delta_{\mathrm{t}}^{2}} \tag{4}$$

where δ_{n}, δ_{s} and δ_{t} are the relative normal, longitudinal shear and transverse shear displacements of cohesive elements. $\langle \delta_{\mathrm{n}} \rangle = \delta_{\mathrm{n}}$ when $\delta_{\mathrm{n}} > 0$, otherwise $\langle \delta_{\mathrm{n}} \rangle = 0$. For the linear damage period as shown in Fig.4, the damage variable D can be expressed as

$$D = \frac{\delta_{\mathrm{m}}^{\mathrm{f}}(\delta_{\mathrm{m}}^{\mathrm{m}} - \delta_{\mathrm{m}}^{0})}{\delta_{\mathrm{m}}^{\mathrm{m}}(\delta_{\mathrm{m}}^{\mathrm{f}} - \delta_{\mathrm{m}}^{0})} \tag{5}$$

where $\delta_{\mathrm{m}}^{\mathrm{m}}$ is the maximum displacement when cohesive elements separate; δ_{m}^{0} and $\delta_{\mathrm{m}}^{\mathrm{f}}$ are the relative displacements when damage initiates and tractions diminish, respectively.

The damage evolution of cohesive elements follows the maximum principle stress criterion:

$$\max\left\{\frac{\langle t_{\mathrm{n}} \rangle}{t_{\mathrm{n}}^{0}}, \frac{t_{\mathrm{s}}}{t_{\mathrm{s}}^{0}}, \frac{t_{\mathrm{t}}}{t_{\mathrm{t}}^{0}}\right\} = 1 \tag{6}$$

where $\langle t_{\mathrm{n}} \rangle = t_{\mathrm{n}}$ when $t_{\mathrm{n}} > 0$, otherwise $\langle t_{\mathrm{n}} \rangle = 0$.

3.2 Numerical model and simulation procedure

The numerical models of semi-circular specimens are set up by inserting a zero-thickness cohesive element into two adjacent finite solid elements as shown in Fig.5. The 3D numerical specimen is partitioned into wedge-shaped solid elements with a length of side 1 mm. The geometry of model is set up by inserting 12730 zero-thickness cohesive elements into 8578 wedge-shaped solid elements, as shown in Fig.6. To improve the computational efficiency, the thickness of numerical model is set as 1 mm considering the assumption of plane-stress. The direction of bedding planes is in consistent with the loading direction. In addition, the numerical model has a bedding spacing of 5 mm, a diameter of 100 mm, a notch length of 10 mm and a span-diameter ratio of 0.8. In order to reduce the interference of other factors, the notch tip is set in the rock matrix and the vertical loading rate is set as 0.01 mm/min.

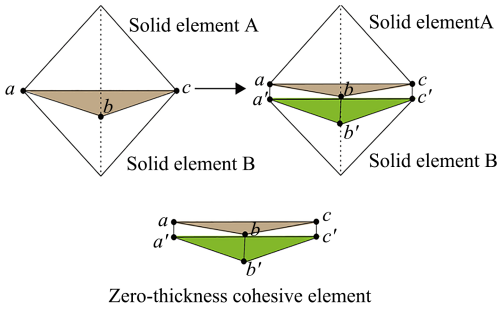

Fig.5 Insertion of cohesive elements into solid elements

3.3 Calibration of micro-parameters in numerical model

It is difficult to obtain the mechanical parameters representing the strength of cohesive elements in experiments, thus it is necessary to calibrate the micro-parameters of cohesive elements in ABAQUS based on macro-mechanical properties obtained from SCB tests. The load-displacement curve and peak load are regarded as the calibration parameters, which are repeatedly adjusted until the numerical results fit well with experimental results. The parameters of cohesive elements after calibration are listed in Table 1.

Figure 7 shows the comparison of load–displacement curves between numerical simulation and experiments based on micro-parameters listed in Table 1. It indicates that the numerical load–displacement curves agree well with those of

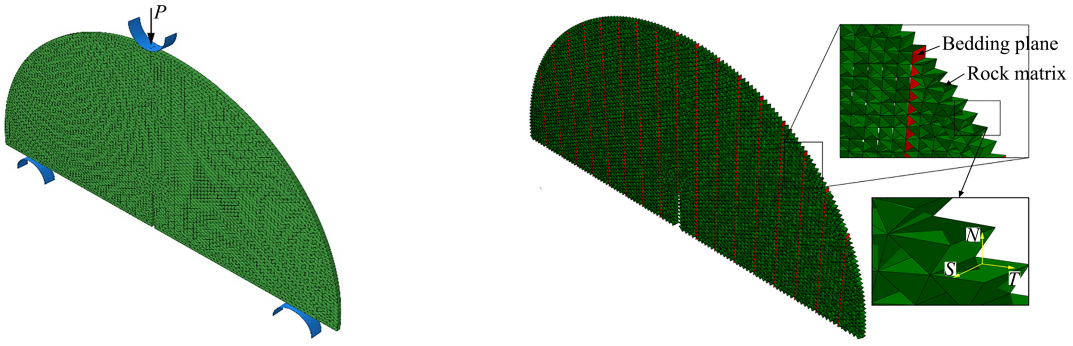

(a) Numerical model and loading condition (b) Cohesive elements

Fig.6 Numerical specimen model

Table 1 Micro-parameters used in the simulation

Element type		Density /(kg • m^{-3})	Elastic modulus/GPa	Poisson's ratio	Normal stiffness (MPa • mm^{-1})	Shear stiffness (MPa • mm^{-1})	Tensile strength/MPa	Shear strength/MPa	Displacement at failure/mm
Rock material		2 437	25	0.23	—	—	10.5	25	—
Cohesive elements	Bedding plane	—	—	—	1 200	4 000	3.0	10	0.05
	Rock matrix	—	—	—	2 400	8 800	6.0	22	0.10

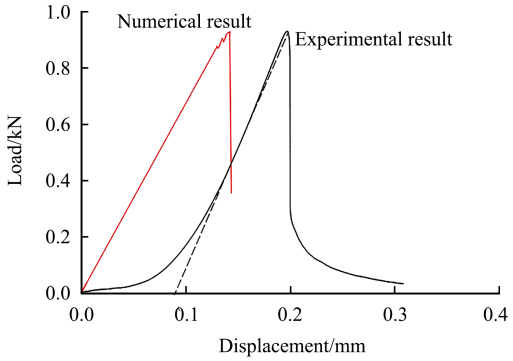

(a) θ= 0°

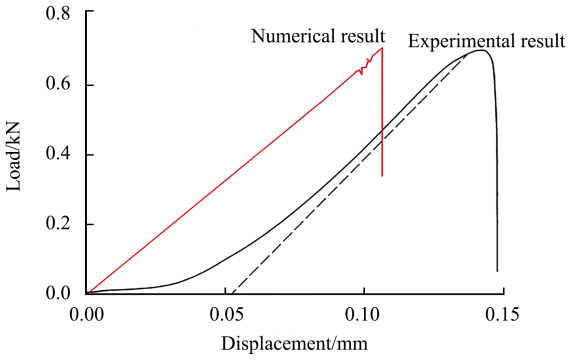

(b) θ= 30°

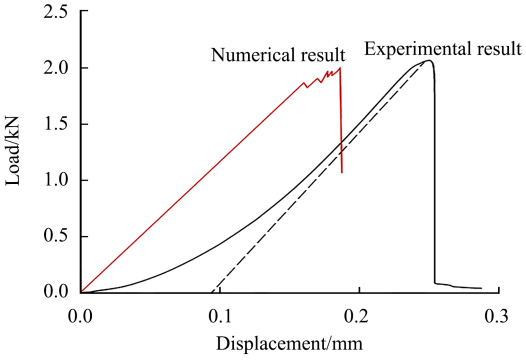

(c) θ= 45°

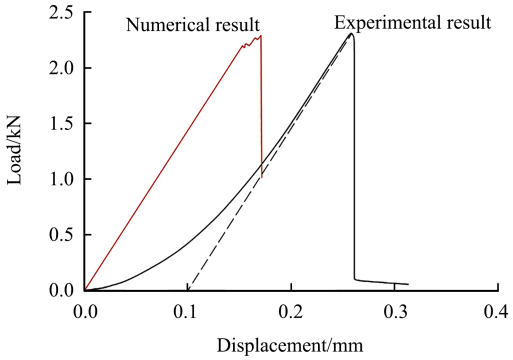

(d) θ= 60°

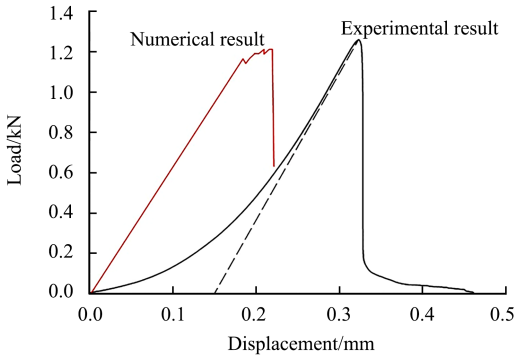

(e) θ= 90°

Fig.7 Comparison between load-displacement curves of numerical and experimental specimens

experimental results at the stages of elastic deformation, peak load and the brittle failure after peak load. However, at the initial stage of loading process, the closure of pre-existing micro-cracks and pores in sandstone causes non-linear deformation of rock specimens, leading to the load–displacement curves to present the downward concave, while this characteristic is not found in numerical simulations[28−29].

3.4 Comparison between numerical and experimental results

The macro-mechanical responses of the SCB specimen under the three-point-bending test, including peak load and fracture pattern, are used to make a comparison between numerical and experimental results.

3.4.1 Peak load

Figure 8 shows a good consistency between the numerical and experimental results on peak loads. It indicates that the peak load increases with the increase of bedding inclination angles.

3.4.2 Fracture pattern

Figure 9 shows the numerical and experimental fracture patterns of specimens with different inclination angles. It should be noted that the value of MMIXDME is the output variable that defines the failure modes (tensile or shear failure) of cohesive elements in the Abaqus code. When MMIXDME = −1, the elements are not at failure. When MMIXDME is between 0 and 0.5, the elements are dominated by tensile failure. The shear failure occurs when MMIXDME is between 0.5 and 1.0. Therefore, the red and the green regions represent elements at shear and tensile failure, respectively, and the gray

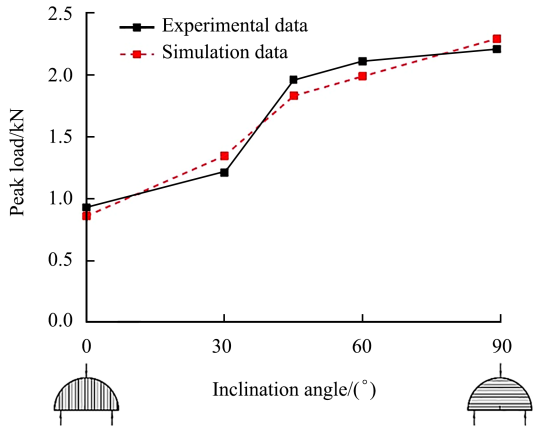

Fig.8 Comparison of peak load for numerical and experimental specimens

parts represent the non-damaged elements in Fig.9. The numerical and experimental results indicate that the specimens with θ=0° are mainly subjected to tensile failure along the bedding planes (Fig.9(a)). The location of rupture plane obtained from experiments deviates from that of numerical results, which may be caused by the difference of bedding strength in the natural rock materials. It ideally assumes that the bedding strength is uniform for each bedding plane in the numerical model. Therefore, tensile failure along the middle bedding plane occurs in the numerical model. The shear failure prevails along the bedding plane for specimens with θ=30°; the tensile failure is mainly along the bedding planes for specimens with θ=45°, while the tensile failure across the bedding planes is the main pattern for specimens with θ=60°–90°. The comparison indicates that numerical simulation results agree basically well with experiments on the fracture path.

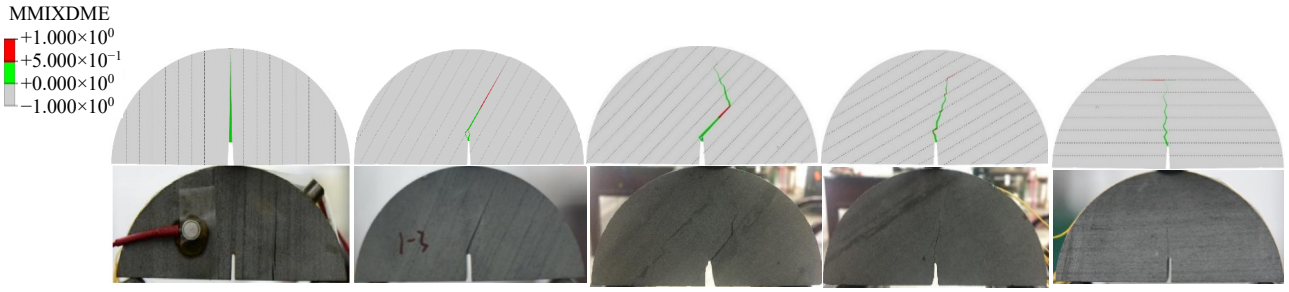

(a) θ = 0° (b) θ = 30° (c) θ = 45° (d) θ = 60° (e) θ=90°

Fig.9 Comparison of numerical and experimental fracture patterns of specimens

The comparison indicates that numerical macro-mechanical response including load–displacement curve, peak load and fracture pattern agrees well with the experimental results. Therefore, the proposed numerical model with the micro-parameters listed in Table 1 can be used to predict the fracture behavior of layered rock specimens under three-point-bending tests.

4 Impacts of bedding strength on the fracture behavior of specimens

The strength of bedding plane is related to diagenetic process. It is difficult to quantitatively reflect the difference in the tested natural rock samples. Therefore, it is necessary to conduct numerical simulation to investigate the effects of bedding strength on the fracture behavior of SCB specimens. By altering the tensile and shear strengths of the bedding plane simultaneously, numerical models of specimens with different bedding strengths and different bedding inclination angles are set up. With strength ratios of 1.25, 1.00, 0.75, 0.50 to the calibrated bedding strength listed in Table 1, four sets of parameters on bedding plane strength are obtained and adopted in the simulation. All the other parameters shown in Table 1 keep constant.

4.1 Fracture toughness

The fracture toughness of specimens with various bedding strengths is shown in Fig.10. It shows that the fracture toughness increases with the increase of bedding inclination angles and the increasing trend is rather obvious when the bedding inclination angle is small. In addition, the influence of bedding strength on the fracture toughness is larger at much smaller bedding inclination angles. The fracture toughness of specimens increases obviously with the increase of bedding strength.

4.2 Fracture pattern

Figure 11 shows the numerical fracture patterns for SCB specimens with different bedding strength. It indicates that the fracture pattern of specimens is not influenced by the bedding strength and the specimens are subjected to tensile failure along the vertical bedding planes when θ=0° (Fig.11(a)). For specimens with θ=30°–90°, when the bedding strength ratio equals to 1.25:1.00, specimens at these bedding inclination angles are dominated by tensile failure, but the fracture path differs. The specimens with θ=30°–45° are dominated by

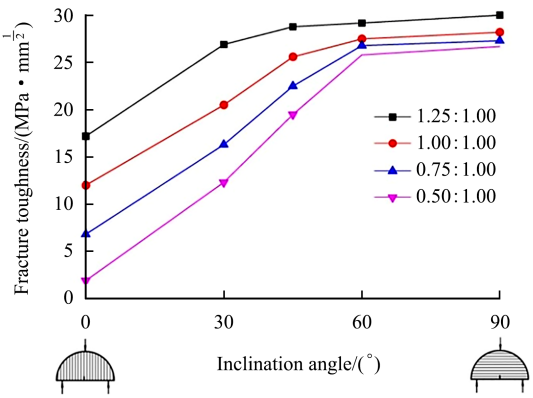

Fig.10 Numerical fracture toughness of specimens with different bedding strength

tensile failure along the bedding planes (Figs.11(b) and 11(c)). While specimens with θ=60°–90° are dominated by tensile failure across the bedding planes (Figs.11(d) and 11(e)). When the bedding strength ratio is 1.00:1.00, the specimens with θ=30° are dominated by shear failure along the bedding planes. A few shear cracks along the bedding planes start to appear on specimens with other bedding inclination angles (i.e., 0°, 45°, 60°, 90°). The specimens are still dominated by tensile failure across the bedding planes. The lengths of cracks along the bedding planes under specific bedding strength are larger than that of specimens with the bedding strength ratios of 1.25:1.00. When the bedding strength ratio is 0.75:1.00, the specimens with θ=30°–60° are dominated by tensile failure along the

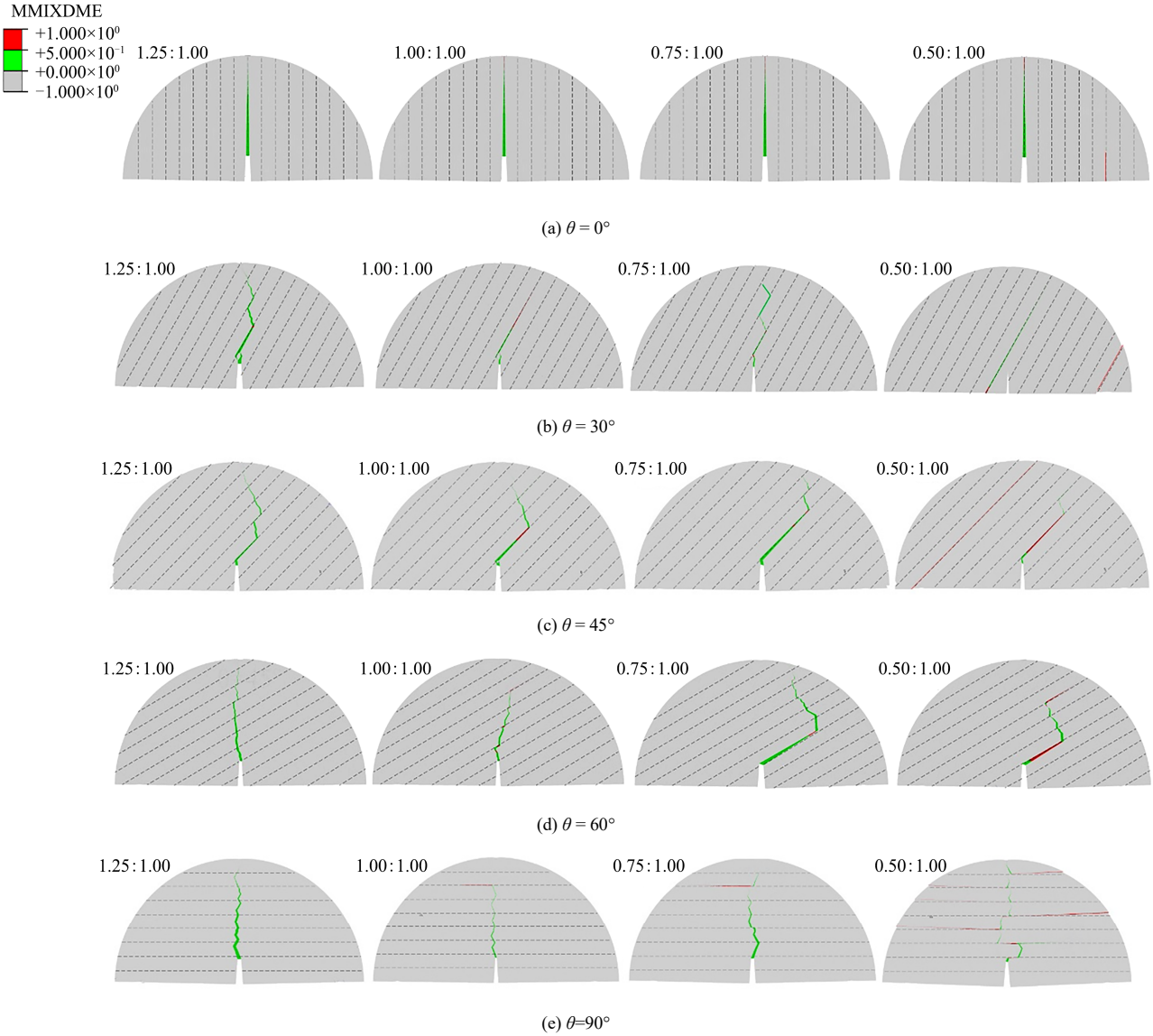

Fig.11 Numerical fracture patterns of specimens with different bedding strength

bedding planes. The proportion of shear cracks is not obvious but the length of cracks along the bedding plane increases obviously (Figs.11(b), 11(c) and (d)). The specimens with θ=90° are dominated by tensile failure across the bedding planes and a few shear cracks occur along the bedding plane (Fig.11(e)). When the bedding strength ratio is 0.50:1.00, specimens with θ=30° are dominated by tensile failure along the bedding planes (Fig.11(b)) and specimens with θ=45°–90°

are dominated by shear failure along the bedding planes, and accompanied by a few tensile cracks across the bedding planes (Figs.11(c), d and 11(e)). The proportion of shear cracks on specimens with θ=45° is even more than 80%. From the above analysis, it implies that the fracture patterns of specimens are not only influenced by the bedding strength, but also controlled by the bedding inclination angles. The fracture pattern of specimens with θ=0° is not influenced by the bedding strength. The specimens with θ=30° are dominated by shear failure along the bedding planes when the bedding strength ratio is 1.00:1.00 and tensile failure along the bedding planes dominates in specimens with other bedding strength ratios. When the bedding strength is larger (1.25:1.00–1.00:1.00), specimens with θ=45° are dominated by tensile failure along the bedding planes while specimens with θ=60°–90° are dominated by tensile failure across the bedding planes. When the bedding strength is small (0.75:1.00–0.50:1.00), the length of cracks along the bedding planes on the specimens presents an apparent increase and the fracture pattern changes gradually from tensile failure to shear failure. When the bedding strength ratio is 0.50:1.00, specimens with θ=45°–90° are dominated by shear failure along the bedding planes. Comparison of the fracture paths on specimens with various bedding strengths indicates that the lower bedding strength at each bedding inclination angle may induce larger length of cracks along the bedding planes except the case of specimens with θ=0°.

To describe the effects of bedding strength on the fracture patterns of specimens more clearly, the failure mode of the contact elements (micro-cracks) are also statistically analyzed as shown in Fig.12. The results indicate that when the bedding strength is relatively large (Figs.12(a) and 12(b)), the specimens at various bedding inclination angles are all dominated by tensile failure and the crack propagation direction is almost uniform with the loading direction. When the bedding strength ratio is 0.75:1.00 (Fig.12(c)), the number of elements subjected to shear failure on specimens with θ=30°–90° increases

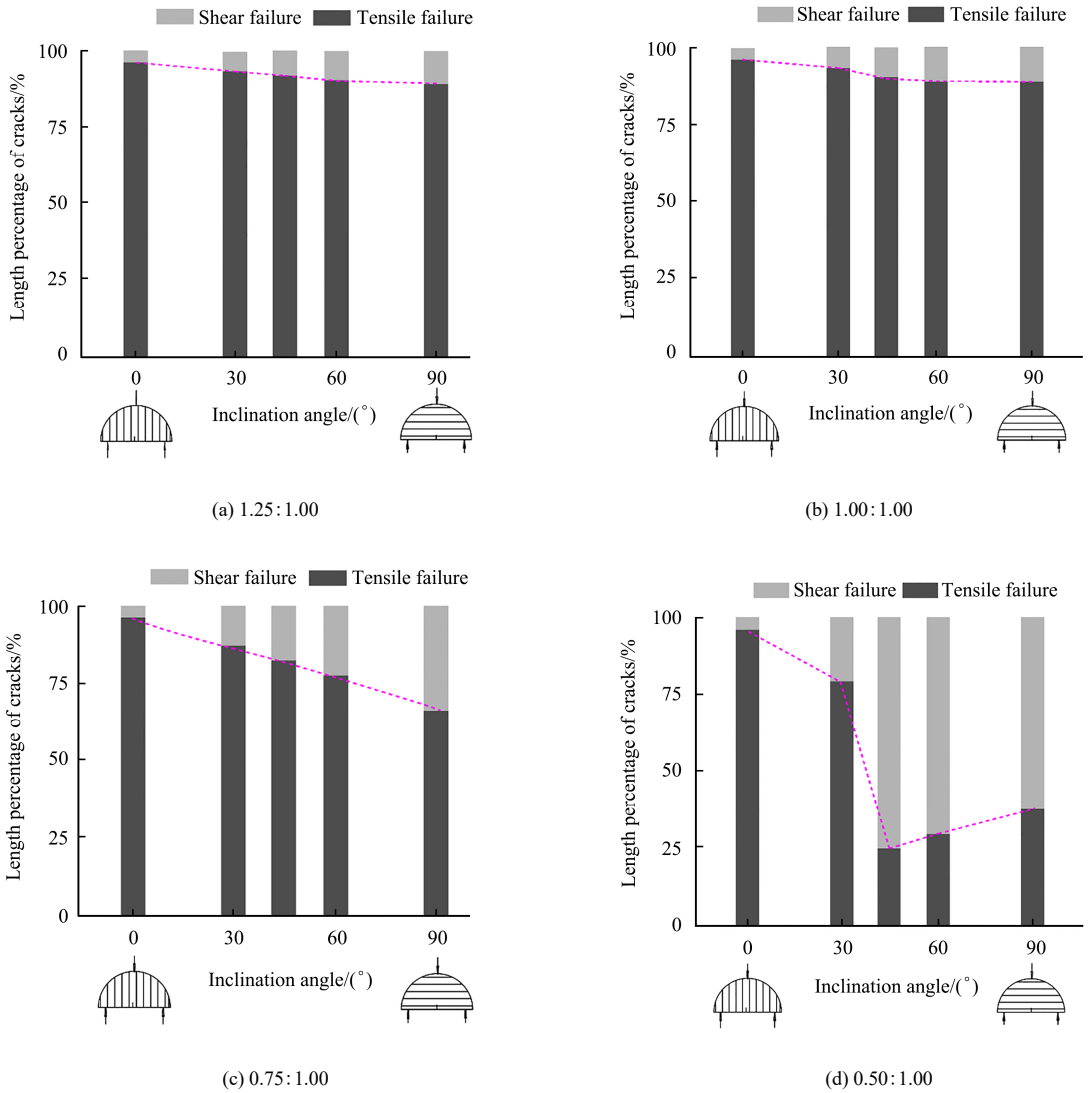

(a) 1.25∶1.00 (b) 1.00∶1.00

(c) 0.75∶1.00 (d) 0.50∶1.00

Fig.12 Percentage of cracks under different bedding strengths

markedly, which may be attributed to the inter-layer slipping caused by much lower bedding strength, but the specimens are still dominated by tensile failure. When the bedding strength ratio decreases to 0.50:1.00 (Fig.12(d)), a significant increase occurs in the number of shear cracks on specimens with θ=45°–90°, implying the inter-layer slipping exacerbates. Especially for specimens with θ=45°, the length percentage of shear cracks even reaches 80%. While the specimens with θ=0° are always dominated by tensile failure and the failure mode is not influenced by the bedding strength. The above analysis indicates that the failure mode is not only related to the bedding strength, but also controlled by bedding inclination angles.

4.3 Initiation angle

Based on the numerical results shown in Fig.11, the initiation angles of specimens with various inclination angles under different bedding strength are shown in Table 2 (the value of initiation angle is defined as positive when it is anticlockwise from the loading direction and negative when it is clockwise). It indicates that the initiation angle equals to 0° when θ=0°, while for specimens with θ=30°, the initiation angle increases with the decrease of bedding strength. The initiation direction of specimen with the bedding strength ratio of 1.25:1.00 is contrary to those at other bedding strength ratios. Initiation angles on specimens with θ=45°–90° decrease firstly and then increase with the decrease of bedding strength and the initiation direction diverts from the left side of the loading axis to the ride side gradually. The variation is described in detail as follows: the initiation angle of the specimens with θ=45° approaches 0° when the bedding strength ratio is 0.75:1.00 and the initiation angle becomes negative when the bedding strength ratio is 0.50:1.00, which is contrary to those with other bedding strength ratios. The initiation angles on specimens with θ=60° changes markedly with the decrease of bedding strength. The values of initiation angles become positive when the bedding strength is relatively large (1.25:1.00–1.00:1.00); the values of initiation angles become negative and the initiation direction deviates towards the right side of the loading axis and is close to the bedding orientation when the bedding strength is relatively small (0.75:1.00–0.50:1.00). For the specimens with θ=90°, the initiating direction slightly deviates towards the left side of the loading axis and the initiation angle approaches 0° when the bedding strength is relatively large (1.25:1.00–1.00:1.00). When the bedding strength is relatively small (0.75:1.00–0.50:1.00), the initiating direction starts to offset towards the right side of the loading axis and the initiation angle increases markedly.

Table 2 Crack initiation angles of specimens with different bedding strength obtained from simulations

Bedding inclination angle(°)	Initiation angle/(°)			
	Bedding strength 1.25:1.00	Bedding strength 1.00:1.00	Bedding strength 0.75:1.00	Bedding strength 0.50:1.00
0	0.0	0.0	0.0	0.0
30	12.0	−28.0	−29.5	−30.0
45	18.0	10.0	3.0	−10.0
60	8.0	4.5	−50.0	−59.6
90	3.5	2.0	−8.0	−9.2

4.4 Crack propagation path

Based on the fracture patterns and propagation paths of specimens obtained from numerical simulations, statistics of the length of cracks along the bedding planes of specimens with different bedding inclination angles and different bedding strengths are shown in Fig.13. It can be seen that the percentage of crack length along the bedding planes decreases with the increase of bedding inclination angles. The crack propagation path on specimens with θ=0° is basically not affected by the bedding strength. For the specimens with θ=30°–90°, the length of cracks along the bedding planes is much larger when the bedding strength is relatively small (0.75:1.00–0.50:1.00) than that of the bedding strength is relatively large (1.25:1.00–1.00:1.00). The impacts of decrease in bedding strength on the percentage crack length along the bedding planes is much larger for specimens with larger bedding inclination angles. The percentage of crack length along the bedding planes even reaches about 80% for specimens with θ=90° when the bedding strength ratio is 0.50:1.00. Therefore, both the bedding strength and inclination angle dominate the crack propagation path.

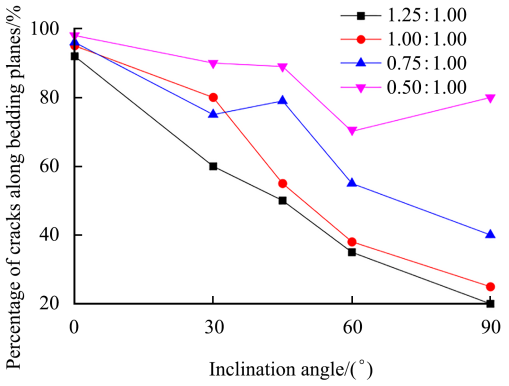

Fig.13 Percentage of crack length along bedding direction in specimens with different bedding strength

5 Conclusions

The cohesive element model presented in this paper has

been verified by experiments and it is applicable to simulating the fracture behavior of sandstone specimens with different bedding inclination angles under three-point-bending tests. It is able to obtain the macro fracture characteristics such as crack initiation and propagation, peak load and fracture patterns of the fracture process.

The fracture toughness of the sandstone increases with the increase of bedding inclination angle at the same bedding strength, and the variation is obvious when the bedding inclination angle is small, which has been verified by the experiments. Generally, the fracture toughness of the specimen increases with the increase of bedding strength, but the extent of the impact is different with the bedding inclination angles. The influence of bedding strength on the fracture toughness is more significant when the bedding inclination angle of the specimen is smaller.

The fracture patterns of sandstone specimens are not only related to the bedding strength, but also controlled by the bedding inclination angles. For specimens with θ=0°, the fracture patterns are basically not affected by the bedding strength. The shear failure occurs mainly along the bedding planes when the bedding strength ratio is 1.00:1.00 for specimens with θ=30°, while tensile failure prevails along the bedding planes with other bedding strength ratios. When the bedding strength is relatively large (1.25:1.00–1.00:1.00), specimens with θ=45° are dominated by tensile failure along the bedding planes and specimens with θ=60°–90° are dominated by tensile failure across the bedding planes. When the bedding strength is relatively small (0.75:1.00–0.50:1.00), the fracture patterns gradually change from tensile failure to shear failure. The specimens with θ=45°–90° are all dominated by shear failure along the bedding planes when the bedding strength ratio is 0.50:1.00. In addition, by comparing the fracture paths of specimens with different bedding strengths, it is found that the length of cracks along the bedding planes is much larger for specimens with lower bedding strength and the specific bedding inclination angle except the case of θ=0°.

For specimens with θ=0°, the initiation angle is 0°. For specimens with θ=30°, the initiation angle increases with the decrease of bedding strength, and the initiation direction of specimens with the bedding strength ratio of 1.25:1.00 is contrary to other specimens with different bedding strength ratios. For the specimens with θ=45°–90°, the initiation angle firstly decreases and then increases with the decrease of bedding strength and the initiating direction deviates gradually from the left side of the loading axis to the right side .

By comparing the crack propagation paths of specimens under different bedding strengths, it is found that the length percentage of cracks along the bedding planes decreases generally with the increase of bedding inclination angles and the crack propagation path on specimens with θ=0° is not affected by the bedding strength. For the specimens with θ=30°–90°, the length of cracks along the bedding planes of specimens with lower bedding strength (0.75:1.00–0.50:1.00) are more than that of the specimens with a much higher bedding strength (1.25:1.00–1.00:1.00). In addition, the percentage of crack length along the bedding plane direction is more easily affected by the bedding strength when the bedding inclination angle is much larger.

Reference

[1] ABBASS T, ANDRE V. Effect of layer orientation on the failure of layered sandstone under Brazilian test conditions[J]. International Journal of Rock Mechanics and Mining Sciences, 2010, 47: 313−322.

[2] CHEN CS, PAN E, AMADEI B. Determination of deformability and tensile strength of anisotropic rock using Brazilian tests[J]. International Journal of Rock Mechanics and Mining Sciences, 1998, 35(1): 43−61.

[3] DEBECKER B, VERVOORT A. Experimental observation of fracture patterns in layered slate[J]. International Journal of Fracture, 2009, 159: 51−62.

[4] CHO J W, KIM H, JEON S, et al. Deformation and strength anisotropy of Asan gneiss, Boryeong shale, and Yeoncheon schist[J]. International Journal of Rock Mechanics and Mining Sciences, 2012, 50(2): 158−169.

[5] LIU Yun-si, FU He-lin, RAO Jun-ying, et al. Research on Brazilian disc splitting tests for anisotropy of slate under influence of different bedding orientations[J]. Chinese Journal of Rock Mechanics and Engineering, 2012, 31(4): 785−791.

[6] LI Zhi-gang, XU Guang-li, HUANG Peng, et al. Mechanical and anisotropic properties of silty slates[J]. Rock and Soil Mechanics, 2018, 39(5): 1737−1746.

[7] TENG Jun-yang, TANG Jian-xin, ZHANG Chuang. Experimental study on tensile strength of layered water-bearing shale[J]. Rock and Soil Mechanics, 2018, 39(4): 1317−1326.

[8] LIU Sheng-li, CHEN Shan-xiong, YU Fei, et al. Anisotropic properties study of chlorite schist[J]. Rock and Soil Mechanics, 2012, 33(12): 3616−3623.

[9] CHONG K P, KURUPPU M D. New specimen for fracture toughness determination of rock and other

materials[J]. International Journal of Fracture, 1984, 26: 59−62.

[10] LIM I L, JOHNSTON I W. Fracture Testing of a soft rock with semi-circular specimens under three-point bending. Part 1-Mode I[J]. International Journal of Rock Mechanics and Mining Sciences, 1994, 31(3): 185−197.

[11] LIM I L, JOHNSTON I W. Stress intensity factors for semi-circular specimens under three-point bending[J]. Engineering Fracture Mechanics, 1993, 44(3): 363−382.

[12] KURUPPU M D, OBARA Y, AYATOLLAHI M R. ISRM-suggested method for determining the mode I static fracture toughness using semi-circular bend specimen[J]. Rock Mechanics and Rock Engineering, 2014, 47: 267−274.

[13] WEI M D, DAI F, XU N W, et al. Experimental and numerical study on the fracture process zone and fracture toughness determination for ISRM suggested semi-circular bend rock specimen[J]. Engineering Fracture Mechanics, 2016, 154: 43−56.

[14] NATHAN DUTLER, MORTEZA NEJATI. On the link between fracture toughness, tensile strength, and fracture process zone in anisotropic rocks[J]. Engineering Fracture Mechanics, 2018, 201: 56−79.

[15] KATAOKA M, OBARA Y, KURUPPU M. Estimation of fracture toughness of anisotropic rocks by semi-circular bend (SCB) tests under water vapor pressure[J]. Rock Mechanics and Rock Engineering, 2015, 48: 1353−1367.

[16] MICHAEL R C. Fracture toughness anisotropy in shale[J]. Journal of Geophysical Research, 2016, 121: 1−16.

[17] CHONG K P, KURUPPU M D, KUSZMAUL J S. Fracture toughness determination of layered materials[J]. Engineering Fracture Mechanics, 1987, 28: 43−54.

[18] XU W, CAO P. Fracture behaviour of cemented tailing backfill with pre-existing crack and thermal treatment under three-point bending loading: experimental studies and particle flow code simulation[J]. Engineering Fracture Mechanics, 2018, 195(1): 129−141.

[19] MENG W, YAO Y, MOBASHER B, et al. Effects of loading rate and notch-to-depth ratio of notched beams on flexural performance of ultra-high-performance concrete[J]. Cement and Concrete Composites, 2017, 83(10): 349−359.

[20] HOU P, FAN Z, ZHANG L, et al. Failure mechanism of brass with three V-notches characterized by acoustic emission in in situ three-point bending tests[J]. Advanced Engineering Materials, 2016, 18(12): 1−10.

[21] BIANI N. Discrete element methods. Encyclopedia of computational mechanics[M]. [S. l.]: John Wiley & Sons Ltd., 2004.

[22] LEE H P, OLSON J E, SCHULTZ R A. Interaction analysis of propagating opening mode fractures with veins using the discrete element method[J]. International Journal of Rock Mechanics and Mining Sciences, 2018, 103(3): 275−288.

[23] MANOUCHEHRIAN A, MARJI M F. Numerical analysis of confinement effect on crack propagation mechanism from a flaw in a pre-cracked rock under compression[J]. Acta Mechanica Sinica, 2012, 28(5): 1389−1397.

[24] JIANG H X, MENG D G. 3D numerical modelling of rock fracture with a hybrid finite and cohesive element method[J]. Engineering Fracture Mechanics, 2018, 199(8): 280−293.

[25] JAIME M C, ZHOU Y, LIN J S, et al. Finite element modeling of rock cutting and its fragmentation process[J]. International Journal of Rock Mechanics and Mining Sciences, 2015, 80(12): 137−146.

[26] MENEZES P L, LOVELL M R, AVDEEV I V, et al. Studies on the formation of discontinuous chips during rock cutting using an explicit finite element model[J]. International Journal of Advanced Manufacturing Technology, 2014, 70(1): 635−648.

[27] WANG H Y. Numerical modeling of non-planar hydraulic fracture propagation in brittle and ductile rocks using XFEM with cohesive zone method[J]. Journal of Petroleum Science and Engineering, 2015, 135(11): 127−140.

[28] JIANG H X, MENG D G. 3D numerical modelling of rock fracture with a hybrid finite and cohesive element method[J]. Engineering Fracture Mechanics, 2018, 199(8): 280−293.

[29] DOU F K, WANG J G, ZHANG X X, et al. Effect of joint parameters on fracturing behavior of shale in notched three-point-bending test based on discrete element model[J]. Engineering Fracture Mechanics, 2019, 205(1): 40−56.